validation studies using oxygen-15-water and PET. *J Nucl Med* 1993; 34 (3): 498–505.
32. Ichise M, Toyama H, Innis R, Carson R. Strategies to improve neuroreceptor parameter estimation by linear regression analysis. *J Cereb Blood Flow Metab* 2002; 22 (10): 1271–1281.
33. Slifstein M, Laruelle M. Effects of statistical noise on graphic analysis of PET neuroreceptor studies. *J Nucl Med* 2000; 41 (12): 2083–2088.
34. Gunn R, Lammertsma A, Hume S, Cunningham V. Parametric imaging of ligand-receptor binding in PET using a simplified reference region model. *Neuroimage* 1997; 6 (4): 279–287.
35. Watabe H, Watabe H, Jino H, Jino H, Kawachi N, Kawachi N, et al. Parametric imaging of myocardial blood flow with ^{15}O-water and PET using the basis function method. *J Nucl Med* 2005; 46 (7): 1219–1224.
36. Breier A, Su T, Saunders R, Carson R, Kolachana B, Bartolomeis de A, et al. Schizophrenia is associated with elevated amphetamine-induced synaptic dopamine concentrations: evidence from a novel positron emission tomography method. *Proc Natl Acad Sci USA* 1997; 94 (6): 2569–2574.
37. Endres C, Kolachana B, Saunders R, Su T, Weinberger D, Breier A, et al. Kinetic modeling of [^{11}C]raclopride: combined PET-microdialysis studies. *J Cereb Blood Flow Metab* 1997; 17 (9): 932–942.
38. Koeppe R, Raffel D, Snyder S, Ficaro E, Kilbourn M, Kuhl D. Dual-[^{11}C]tracer single-acquisition positron emission tomography studies. *J Cereb Blood Flow Metab* 2001; 21 (12): 1480–1492.
39. Kudomi N, Hayashi T, Teramoto N, Watabe H, Kawachi N, Ohta Y, et al. Rapid quantitative measurement of $CMRO_2$ and CBF by dual administration of ^{15}O-labeled oxygen and water during a single PET scan—a validation study and error analysis in anesthetized monkeys. *J Cereb Blood Flow Metab* 2005; 25: 1209–1224.
40. Green L, Nguyen K, Berenji B, Iyer M, Bauer E, Barrio J, et al. A tracer kinetic model for ^{18}F-FHBG for quantitating herpes simplex virus type 1 thymidine kinase reporter gene expression in living animals using PET. *J Nucl Med* 2004; 45 (9): 1560–1570.
41. Richard J, Zhou Z, Chen D, Mintun M, Piwnica-Worms D, Factor P, et al. Quantitation of pulmonary transgene expression with PET imaging. *J Nucl Med* 2004; 45 (4): 644–654.

ORIGINAL ARTICLE

Annals of Nuclear Medicine Vol. 20, No. 3, 189–194, 2006

Performance of list mode data acquisition with ECAT EXACT HR and ECAT EXACT HR+ positron emission scanners

Hiroshi WATABE,* Keiichi MATSUMOTO,** Michio SENDA** and Hidehiro IIDA*

*Department of Investigative Radiology, National Cardiovascular Center Research Institute
**Institute of Biomedical Research and Innovation

Recently, list mode (event-by-event) data acquisition with positron emission tomography (PET) has been widely noticed because list mode acquisition is superior to conventional frame mode data acquisition in terms of (1) higher efficiency of data storage, (2) higher temporal resolution, and (3) higher flexibility of data manipulation. The aim of this study is to investigate the performance of list mode data acquisition with ECAT EXACT HR and HR+ PET scanners (CTI PET Systems) and its feasibility in clinical applications. A cylindrical phantom (16 cm in diameter and length) filled with a ^{11}C solution for the HR and a ^{15}O solution for the HR+ was scanned several times by varying the radioactivity concentration with the list mode and frame mode acquisitions. The scans were also carried out with a septa (2D mode) and without a septa (3D mode) in order to evaluate the effect of the interplane septa on the quality of the list mode data. The acquired list mode data were sorted into a sinogram and reconstructed using a filtered back-projection algorithm. The count rate performance of the list mode data was comparable to that of the frame mode data. However, the list mode acquisition could not be performed when the radioactivity concentration in the field-of-view was high (exceeding 24 kBq/m*l* for the 3D mode) due to a lack of sufficient transfer speed for sending data from the memory to hard disk. In order to estimate the pixel noise in a reconstructed image, ten replicated data sets were generated from one list mode data. The reconstructed images with the 3D mode had a signal-to-noise ratio that was more than 60% better than that of the image with the 2D mode. The file size of the generated list mode data was also evaluated. In the case of ECAT EXACT HR+ with the 3D list mode, the list mode data with a generated file size of 2.31 Mbytes/s were generated for 37 MBq injections. Our results suggest that careful attention must be paid to the protocol of the list mode data acquisition in order to obtain the highest performance of the PET scanner.

Key words: PET, list mode, frame mode

INTRODUCTION

RECENTLY, list mode (event-by-event) data acquisition with positron emission tomography (PET) has attracted the attention of many investigators from different fields. In the list mode acquisition, every detected event (both prompt and random) including the location of the line of response in the tomograph is recorded. Although list mode acquisition requires more computational power to process data in comparison to conventional frame mode acquisition, it has several advantages such as (1) higher efficiency of data storage, (2) higher temporal resolution and (3) higher flexibility of data manipulation (flexible frame rebinning, flexible for iterative image reconstruction). Further, many clinical benefits can be expected from the list mode acquisition, for example, real-time motion correction[1,2] and improvement of image quality.[3] However, as compared to the conventional frame mode acquisition, several considerations such as reliability and compatibility must be taken into account before applying

Received August 1, 2005, revision accepted December 6, 2005.

For reprint contact: Hiroshi Watabe, Ph.D., Department of Investigative Radiology, National Cardiovascular Center Research Institute, 5–7–1 Fujishiro-dai, Suita, Osaka 565–8565, JAPAN.

E-mail: watabe@ri.ncvc.go.jp

the list mode acquisition for daily clinical routines.

ECAT EXACT HR[4] and ECAT EXACT HR+[5] (CTI/Siemens, Knoxville, TN, USA) are commercially available PET scanners, which are designed for high spatial resolution, and are employed for research as well as clinical purposes. The goal of this study is to evaluate the performance of the list mode acquisition with ECAT EXACT HR and HR+ scanners and investigate the feasibility of the list mode acquisition in clinical applications. We performed a series of scans of a phantom with the list and frame modes. In order to evaluate the effect of interplane septa on the quality of the list mode data, the scans were carried out with a septa (2D mode) and without a septa (3D mode). The performance of the list mode data acquisition was evaluated with respect to count rate performance, noise property, and generated file size.

MATERIALS AND METHODS

Scanner Description

Table 1 shows the system characteristics of the ECAT EXACT HR scanner in comparison to those of the ECAT EXACT HR+ scanner. Both the scanners have a retractable interplane septa and allow scanning in the 2D mode (with septa) as well as the 3D mode (without septa). For the list mode acquisition, the scanners have a memory of 32 Mbytes for the purpose of gate acquisition. The memory is partitioned into two 16 Mbytes buffers that increment, fill, and write to a hard disk alternately.

Phantom Experiments

We performed phantom experiments for the ECAT EXACT HR scanner at the BF Research Institute (Suita, Osaka, Japan) and ECAT EXACT HR+ scanner at the Institute of Biomedical Research and Innovation (Kobe, Hyogo, Japan). Cylindrical phantoms with a diameter and height of 16 cm were employed for the experiments. A radioactive solution was filled in the phantom and a series of scans were performed with the 2D list, 3D list, 2D frame and 3D frame modes (Table 2). For the EXACT HR scanner, a ^{11}C solution was used, and the duration of each scan was 180 s. For the EXACT HR+ scanner, a ^{15}O solution was used, and the duration of each scan was 30 s. The configurations were different because the experiments were carried out in different institutes using their respective isotopes.

Data Analysis

The obtained list mode data were sorted into sinogram data with a system default span and a maximum ring difference for each scanner (Table 1). The image of each scan was reconstructed using a filtered back-projection technique with a 6-mm Gaussian filter. For the 3D data set, FORE (Fourier rebinning)[6] was applied prior to the reconstruction. The matrix sizes of the reconstructed image were 128 × 128 × 47 for the ECAT EXACT HR scanner and 128 × 128 × 63 for the ECAT EXACT HR+ scanner. The voxel sizes of the reconstructed image were 1.6 × 1.6 × 3.1 mm for the ECAT EXACT HR scanner and 1.6 × 1.6 × 2.4 mm for ECAT EXACT HR+ scanner.

Circular ROIs (regions-of-interest) with a diameter of

Table 1 System characteristics of ECAT EXACT HR in comparison with those of ECAT EXACT HR+ scanners

	HR	HR+
detector ring (slice)	24 (47)	32 (63)
crystals/ring	784	576
block detector design	8 × 7	8 × 8
crystal size (mm)	5.9 × 2.9 × 30	4.39 × 4.05 × 30
axial field-of-view (cm)	15.0	15.5
transaxial field-of-view (cm)	51.4	58.3
element number	336	288
number of angle	392	288
default span (2D)	11	15
default span (3D)	7	9
default maximum ring difference (2D)	5	7
default maximum ring difference (3D)	17	22

Table 2 Summary of the scans performed on the phantom

	HR	HR+
	Radioactivity concentration (kBq/m*l*)	Radioactivity concentration (kBq/m*l*)
2D list mode	85.9	135*
	56.1	71.2
	49.8	39.9
	19.4	22.4
	12.4	11.7
3D list mode	24.5*	32.7*
	23.6	21.2
	15.2	14.1
	10.1	13.8
		11.3
		7.65
		5.23
		4.19
2D frame mode	38.8	121
	36.6	61.0
	8.05	30.9
		15.6
		11.1
3D frame mode	19.0	50.4
	15.0	25.5
		12.9
		6.54
		3.31

Radioactivity in the cylindrical phantom when a scan was initiated is shown. * indicates that data are incomplete due to the lack of transfer speed for sending data to the hard disk.

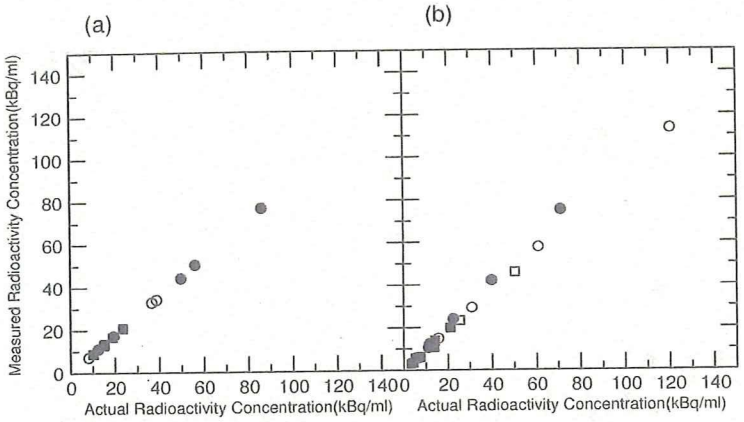

Fig. 1 Comparison of the actual radioactivity concentration inside the phantom and estimated radioactivity concentration from the reconstructed PET image for the ECAT EXACT HR scanner (a) and ECAT EXACT HR+ scanner (b). The filled circles represent the data from the 2D list mode; filled squares, 3D list mode; open circles, 2D frame mode; and open squares, 3D frame mode.

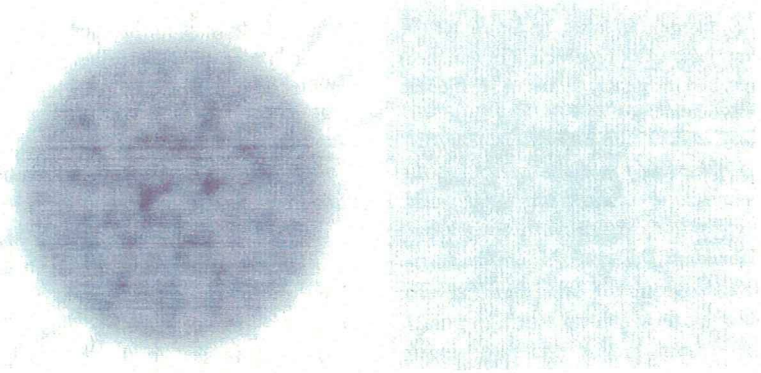

Fig. 2 An example of a generated mean image (*left*) and standard deviation (SD) image (*right*) from 10 replicated data sets generated from one list mode data.

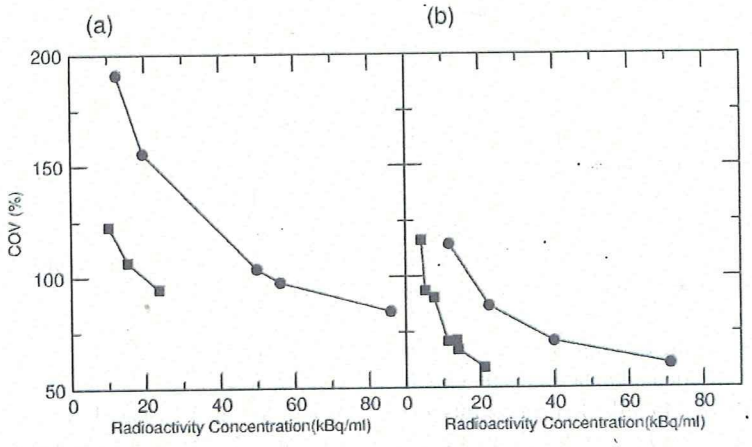

Fig. 3 Relationship between the radioactivity concentration (kBq/ml) and mean coefficient of variance (COV) (%) of the pixel count in the reconstructed image for the ECAT EXACT HR scanner (a) and ECAT EXACT HR+ scanner (b). The lines with filled circles represent the data from the 2D list mode and lines with filled squares represent the data from the 3D list mode.

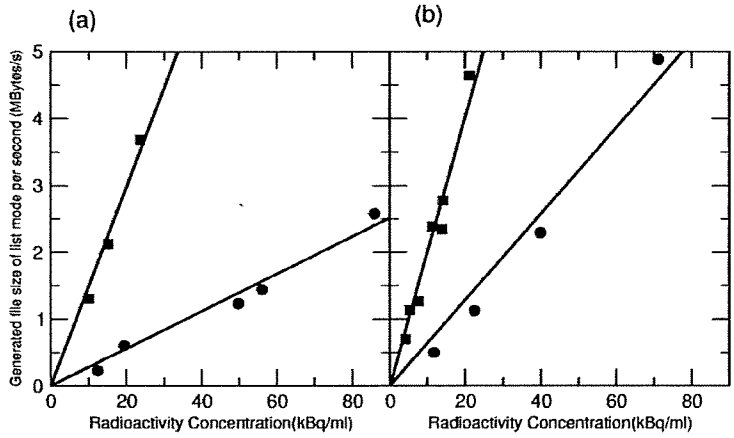

Fig. 4 Relationship between radioactivity concentration (kBq/m*l*) and list mode file size (Mbytes/s) for the ECAT EXACT HR scanner (a) and ECAT EXACT HR+ scanner (b). The filled circles represent the data from the 2D list mode and filled squares represent the data from the 3D list mode. The fitted lines of regression for the data are also shown.

Table 3 Radioactivity concentration in the phantom, NECR (noise equivalent count rate) and COV (coefficient of variance) of the reconstructed image, and the generated list mode file size for the ECAT EXACT HR scanner

Radioactivity concentration (kBq/m*l*)	NECR (/s)	COV (%)	Generated file size per second (Mbytes/s)
	2D list mode		
85.9	9.210×10^4	84.37	2.578
56.1	7.106×10^4	97.32	1.443
49.8	6.423×10^4	103.5	1.234
19.4	4.526×10^4	155.7	0.6034
12.4	1.924×10^4	191.0	0.2279
	3D list mode		
23.6	1.971×10^5	94.57	3.675
15.2	1.465×10^5	106.6	2.123
10.1	1.139×10^5	122.8	1.304

Table 4 Radioactivity concentration in the phantom, NECR and COV of the reconstructed image, and the generated list mode file size for the ECAT EXACT HR+ scanner

Radioactivity concentration (kBq/m*l*)	NECR (/s)	COV(%)	Generated file size per second (Mbytes/s)
	2D list mode		
71.2	1.172×10^5	60.61	4.881
39.9	8.341×10^4	70.73	2.292
22.4	5.470×10^4	86.79	1.124
11.7	3.371×10^4	114.4	0.5012
	3D list mode		
21.2	2.934×10^5	59.05	4.638
14.1	2.331×10^5	67.00	2.779
13.8	1.911×10^5	71.16	2.341
11.3	1.933×10^5	70.76	2.385
7.65	1.214×10^5	90.47	1.263
5.23	1.140×10^5	93.62	1.131
4.19	7.689×10^4	116.1	0.7026

16 cm were placed on the reconstructed image, and the average radioactivity concentration (kBq/m*l*) in the phantom was obtained for each scan.

The NECR (noise equivalent count rate) for each list mode datum was calculated by taking into account the true coincident count rate, random coincident count rate, and scatter fraction in the list mode data.

In order to estimate the noise in a pixel of the reconstructed PET image, 10 replicated data sets were generated from one list mode data. In order to achieve this, the sorting software was modified to produce statistically equivalent multiple sinogram data by splitting the list mode data into pieces. The mean and standard deviation (sd) images were computed from ten reconstructed images. The circular ROIs were placed on both the mean and sd images, and the averaged mean value ($\bar{m}$) and the averaged sd value ($\bar{s}$) were computed. The average COV (coefficient of variance) for each scan was computed from $\bar{m}$ and $\bar{s}$ by considering the physical decay of a radioisotope as follows:

$$\mathrm{COV} = \frac{\bar{s}}{\bar{m}} \cdot \sqrt{\frac{\lambda}{1 - \exp(-\lambda T)}} \times 100\ (\%) \qquad (1)$$

where λ is the physical decay constant (s^{-1}) (0.00567 for ^{15}O and 0.000567 for ^{11}C), and T is the scan duration.

The generated file size of the list mode data per second, S (Mbytes/s), was computed for each list mode scan by considering the physical decay of a radioisotope as follows:

$$S = \frac{F\lambda}{1 - \exp(-\lambda T)} \quad (2)$$

where F (Mbytes) is the generated file size of the list mode data.

RESULTS

Figure 1 (a and b) shows the comparison between the actual radioactivity concentration inside the phantom and the estimated radioactivity concentration from the reconstructed PET image for the ECAT EXACT HR and ECAT EXACT HR+ scanners, respectively. As shown in these figures, there is a good agreement between the list mode data and frame mode data. However, as mentioned in Table 2, if the radioactivity in the field-of-view of the scanner is large, the acquisition of the list mode data would fail due to a lack of sufficient transfer speed for sending data to the hard disk.

Figure 2 shows an example of the generated mean and sd images from the list mode data set. Tables 3 and 4 list the summarized results of the radioactivity concentration in the phantom, NECR and COV in the image, and generated file size of the list mode data for the ECAT EXACT HR and ECAT EXACT HR+ scanners, respectively. Figure 3 shows the relationship between the radioactivity concentration in the phantom and COV in the reconstructed image. As shown in this figure, the image with the 3D acquisition mode has a signal-to-noise ratio that is more than 60% better than that of the image with the 2D acquisition mode. Figure 4 shows the relationship between the radioactivity in the phantom and generated file size of the list mode data. We fitted a line of regression between the radioactivity concentration (A (kBq/ml)) and generated file size (S (Mbytes/s)), and the fitted results are as follows:

$S = 2.79 \times 10^{-2} \times A$ for 2D list mode and ECAT EXACT HR
$S = 1.49 \times 10^{-1} \times A$ for 3D list mode and ECAT EXACT HR
$S = 6.43 \times 10^{-2} \times A$ for 2D list mode and ECAT EXACT HR+
$S = 2.01 \times 10^{-1} \times A$ for 3D list mode and ECAT EXACT HR+ (3)

DISCUSSION

Although the list mode acquisition is not a new technique, the techniques related to the list mode acquisition[3,7–9] have recently become popular due to their advantage as powerful computing systems. Besides the several favorable features of list mode data, additional consideration is required if the list mode acquisition is to be routinely carried out in clinical applications.

Tables 3 and 4 list useful information for scheduling a PET scan with the list mode acquisition. For instance, the injected activity for a patient must be carefully determined by considering 1) the upper limitation of radioactivity concentration, 2) noise in the image and 3) generated file size. The more photons are detected, the larger list mode data are generated. Therefore, generated file size is important from the practical point of view, such as limited size of data storage, time consuming data processes and data backup. According to Eq. (3), assuming that the radioactivity concentration in the field-of-view of the scanner is 10 kBq/ml, a study of ^{15}O for 2 min generates 24.3 Mbytes, 130 Mbytes, 56.0 Mbytes, and 175 Mbytes for the HR 2D list mode, HR 3D list mode, HR+ 2D list mode, and HR+ 3D list mode, respectively. In the case of a ^{11}C study for one hour, 428 Mbytes, 2.29 Gbytes, 987 Mbytes, and 3.01 Gbytes of the list mode data are generated for the HR 2D list mode, HR 3D list mode, HR+ 2D list mode, and HR+ 3D list mode, respectively. In the case of ^{18}F study for one hour, 836 Mbytes, 4.46 Gbytes, 1.93 Gbytes and 6.02 Gbytes for HR 2D list mode, HR 3D list mode, HR+ 2D list mode, HR+ 3D list mode, respectively. The file size of the list mode data for the ECAT EXACT HR+ scanner is larger than that for the ECAT EXACT HR scanner and interestingly the file size of the frame mode for ECAT EXACT HR scanner is larger than that for ECAT EXACT HR+ scanner (sizes of the single-frame sinogram data are 6.2 Mbytes, 23.1 Mbytes, 5.2 Mbytes and 19.8 Mbytes for the HR 2D frame mode, HR 3D frame mode, HR+ 2D frame mode, and HR+ 3D frame mode, respectively).

As shown in Figure 3, the pixel noise in the reconstructed image can be estimated from the list mode data; this is one of the advantages of list mode acquisition. Using multiple frames with very short time duration, the pixel noise can be obtained by the frame mode data. However, it is not ideal due to physical decay of the radioisotope during data acquisition. The pixel noise obtained from the list mode data is quantitatively comparable among scanners. This figure suggests that the noise property of the ECAT EXACT HR+ scanner is superior to that of the ECAT EXACT HR scanner. This is due to the ECAT EXACT HR+ scanner having a higher sensitivity than ECAT EXACT HR scanner, although the two scanners have different system configurations (Table 1). Further, the comparison of the two scanners is complicated.

As shown in Figure 1, the count rate performance of the frame mode and list mode are not surprisingly in good agreement with each other. However, a difference might be observed between the two data sets because of the higher temporal resolution of the list mode data; this enables the accurate correction of the dead-time of the detector and physical decay of the radioisotope. We used the ACS-II (an advanced computational system that is dedicated to handle data from the PET scanner) for both ECAT EXACT HR and HR+ scanners, and the maximum speed of data transfer from the memory to hard disk appears to be approximately 6 Mbytes/s. A read/write controller on the ACS-II with a memory of 32 Mbytes is split into two buffers of approximately 16 Mbytes each.

When the list mode data is being stored from buffer 1 to the hard disk, data are simultaneously written to buffer 2. Once buffer 2 is filled, data are then written to buffer 1, and the data in buffer 2 are written to the hard disk. Since the speed of our hard disk is 6 Mbytes/s and a single event of the list mode data comprises 4 bytes, 1.5 M events/s can be handled. On the other hand, it takes 2.6 s to clear the 16 Mbyte memory. Therefore, if the occurrence of events exceeds 1.5 M events/s, the ACS-II cannot handle all the events.

For usual clinical PET studies, the existence of more than 74 MBq of radioactivity (i.e. 23 kBq/m*l* assuming cylinder with 16 cm diameter) in the field-of-view is not frequent. However, not only true events but also random events are stored in the list mode data and the radioactivity outside the field-of-view must also be considered. It should be noted that since all the possible line of responses are recorded in the list mode data, the number of prompt and random events in the list mode data are greater than those in the frame mode data.

Phantom experiments are often performed with NECR plotted against activity concentration in order to determine the maximum performance of the scanner in terms of image quality. The radioactivity concentrations of about 80 kBq/m*l* and 20 kBq/m*l* give the highest NECR in 2D mode and 3D mode for the ECAT EXACT HR scanner, respectively.[4] These numbers are interestingly close to the maximum radioactivity concentration for the list mode acquisition in our experiments (see Table 2). This suggests the image quality with the list mode can be comparable with that with the frame mode.

In order to use the list mode acquisition at a clinical site, it is also important that a PET scanner be capable of promptly showing the reconstructed PET images. Before reconstruction, a sorting process is necessary for the list mode data, which results in a longer reconstruction time than that for the conventional frame mode data (It takes 0.2 s per 1 M byte of the list mode data for sorting using PC with Xeon CPU (2.4 GHz) and 1 G byte physical memory). Because each event in the list mode data is sequentially stored, it is easy to implement a parallel sorting process. In order to accelerate data processing, the sorting of the list mode data can be performed on a PC cluster[10] which is currently available at a low cost.

The list mode acquisition has several advantages over the conventional frame mode acquisition as mentioned in the first section. However, two disadvantages of the list mode acquisition addressed in this paper, namely, upper limitation of radioactivity and large file size, obstruct the applications of the list mode data on a daily basis. These disadvantages will be overcome along with advances in hardware and software.

CONCLUSION

A series of phantom studies revealed the physical characteristics of the list mode data acquisition with ECAT EXACT HR and HR+ scanners. This study suggests that careful attention must be paid to the protocol of the list mode data acquisition in order to obtain the highest performance of the PET scanner in clinical applications.

ACKNOWLEDGMENT

This study was financially supported by the Budget for Nuclear Research of the Ministry of Education, Culture, Sports, Science and Technology, based on the screening and counseling by the Atomic Energy Commission.

REFERENCES

1. Bloomfield PM, Spinks TJ, Reed J, Schnorr L, Westrip AM, Livieratos L, et al. The design and implementation of a motion correction scheme for neurological PET. *Phys Med Biol* 2003; 48 (8): 959–978.
2. Woo SK, Watabe H, Choi Y, Kim KM, Park CC, Bloomfield PM, et al. Sinogram-based motion correction of PET images using optical motion tracking system and list-mode data acquisition. *IEEE Trans Nucl Sci* 2004; 51 (3): 782–788.
3. Nichols TE, Qi J, Asma E, Leahy RM. Spatiotemporal reconstruction of list-mode PET data. *IEEE Trans Med Imaging* 2002; 21 (4): 396–404.
4. Wienhard K, Dahlbom M, Eriksson L, Michel C, Bruckbauer T, Pietrzyk U, et al. The ECAT EXACT HR: Performance of a new high resolution positron scanner. *J Comput Assist Tomogr* 1994; 18 (1): 110–118.
5. Brix G, Zaers J, Adam LE, Bellemann ME, Ostertag H, Trojan H, et al. Performance evaluation of a whole-body PET scanner using the NEMA protocol national electrical manufacturers association. *J Nucl Med* 1997; 38 (10): 1614–1623.
6. Defrise M, Liu X. A fast rebinning algorithm for 3D positron emission tomography using Johns equation. *Inverse Problems* 1999; 15: 1047–1065.
7. Huesman RH, Klein GJ, Moses WW, Qi J, Reutter BW, Virador PR. List-mode maximum-likelihood reconstruction applied to positron emission mammography (PEM) with irregular sampling. *IEEE Trans Med Imaging* 2000; 19 (5): 532–537.
8. Levkovitz R, Falikman D, Zibulevsky M, Ben-tal A, Nemirovski A. The design and implementation of cosem, an iterative algorithm for fully 3-D listmode data. *IEEE Trans Med Imaging* 2001; 20 (7): 633–642.
9. Byrne C. Likelihood maximization for list-mode emission tomographic image reconstruction. *IEEE Trans Med Imaging* 2001; 20 (10): 1084–1092.
10. Watabe H, Woo Sk, Kim KM, Kudomi N, Iida H. Performance improvement of event-based motion correction for PET using a PC cluster. Conference Record of IEEE Trans Nuclear Science and Medical Imaging Coeference, 2003.

ORIGINAL ARTICLE

Annals of Nuclear Medicine Vol. 20, No. 6, 409–416, 2006

Use of a compact pixellated gamma camera for small animal pinhole SPECT imaging

Tsutomu ZENIYA,* Hiroshi WATABE,* Toshiyuki AOI,* Kyeong Min KIM,** Noboru TERAMOTO,* Takeshi TAKENO,* Yoichiro OHTA,* Takuya HAYASHI,* Hiroyuki MASHINO,*** Toshihiro OTA,*** Seiichi YAMAMOTO**** and Hidehiro IIDA*

*Department of Investigative Radiology, Advanced Medical Engineering Center, National Cardiovascular Center Research Institute
**Nuclear Medicine Laboratory, Radiological and Medical Sciences Research Center, Korea Institute Radiological and Medical Sciences
***Molecular Imaging Laboratory, Inc.
****Department of Electrical Engineering, Kobe City College of Technology

Objectives: Pinhole SPECT which permits *in vivo* high resolution 3D imaging of physiological functions in small animals facilitates objective assessment of pharmaceutical development and regenerative therapy in pre-clinical trials. For handiness and mobility, the miniature size of the SPECT system is useful. We developed a small animal SPECT system based on a compact high-resolution gamma camera fitted to a pinhole collimator and an object-rotating unit. This study was aimed at evaluating the basic performance of the detection system and the feasibility of small animal SPECT imaging. ***Methods:*** The gamma camera consists of a 22 × 22 pixellated scintillator array of 1.8 mm × 1.8 mm × 5 mm NaI(Tl) crystals with 0.2-mm gap between the crystals coupled to a 2″ flat panel position-sensitive photomultiplier tube (Hamamatsu H8500) with 64 channels. The active imaging region of the camera was 43.8 mm × 43.8 mm. Data acquisition is controlled by a personal computer (Microsoft Windows) through the camera controller. Projection data over 360° for SPECT images are obtained by synchronizing with the rotating unit. The knife-edge pinhole collimators made of tungsten are attached on the camera and have 0.5-mm and 1.0-mm apertures. The basic performance of the detection system was evaluated with ^{99m}Tc and ^{201}Tl solutions. Energy resolution, system spatial resolution and linearity of count rate were measured. Rat myocardial perfusion SPECT scans were sequentially performed following intravenous injection of ^{201}TlCl. Projection data were reconstructed using a previously validated pinhole 3D-OSEM method. ***Results:*** The energy resolution at 140 keV was 14.8% using a point source. The system spatial resolutions were 2.8-mm FWHM and 2.5-mm FWHM for ^{99m}Tc and ^{201}Tl line sources, respectively, at 30-mm source distance (magnification factor of 1.3) using a 1.0-mm pinhole. The linearity between the activity and count rate was good up to 10 kcps. In a rat study, the left ventricular walls were clearly visible in all scans. ***Conclusions:*** We developed a compact SPECT system using compact gamma camera for small animals and evaluated basic physical performances. The present system may be of use for quantitation of biological functions such as myocardial blood flow in small animals.

Key words: SPECT, pinhole collimator, compact pixellated gamma camera, small animal

INTRODUCTION

SMALL ANIMAL PET (Positron Emission Tomography) or SPECT (Single Photon Emission Computed Tomography) which permits *in vivo* high resolution three-dimensional (3D) imaging of physiological functions in small

Received February 3, 2006, revision accepted May 10, 2006.
For reprint contact: Tsutomu Zeniya, Ph.D., Department of Investigative Radiology, Advanced Medical Engineering Center, National Cardiovascular Center Research Institute, 5–7–1 Fujishiro-dai, Suita, Osaka 565–8565, JAPAN.
E-mail: zeniya@ri.ncvc.go.jp

laboratory animals, facilitates objective assessment of pharmaceutical development and regenerative therapy in pre-clinical trials.[1–6] Small animal PET has been widely used due to high spatial resolution approaching 1 mm.[7–9] SPECT can also offer high-resolution images by attaching a pinhole collimator with a large magnification factor, when the object is placed close to the pinhole.[10–13] Spatial resolution is improved particularly when a small diameter pinhole is employed.[14–17]

However, a conventional pinhole SPECT has two major limitations. One is its poor sensitivity as compared with small animal PET. The sensitivity of pinhole SPECT is in the order of 1/100–1/1,000 of that of small animal PET, depending on the pinhole diameter, but can be improved by positioning the pinhole collimator close to the object, or by using multiple-detector systems or multiple-pinhole systems.[14,15,17,19,20] Another limitation is the non-uniformity of spatial resolution in the reconstructed 3D images. In pinhole SPECT, the spatial resolution is axially blurred with increased distance from the midplane. This non-uniformity of spatial resolution can be improved by complete data acquisition as demonstrated in our earlier study.[18]

Besides high spatial resolution, the SPECT system has several advantages over PET as its operation is simple, and it does not require an on-site radiochemistry laboratory or a cyclotron for producing radiopharmaceuticals. Pinhole SPECT systems are often composed of clinically used SPECT cameras with pinhole collimator.[3–6,10–15,18,20] However, the clinically used SPECT cameras are inappropriate for small animal imaging, largely due to a lack of manufacturing precision. Also they are not readily accessible to most animal research laboratories.[22]

To overcome these drawbacks, several dedicated small animal pinhole SPECT systems using compact high-resolution gamma cameras have been already developed.[23–25] They used 5″ position-sensitive photomultiplier tube (PSPMT) which had the camera active image region of around 100 mm × 100 mm. In this study, we have employed more a compact pixellated gamma camera with active image region of 43.8 mm × 43.8 mm square coupled to 2″ PSPMT and have developed a compact pinhole SPECT system dedicated to small animal imaging. This study was aimed at evaluating the basic physical performances and the feasibility of small animal imaging in this compact SPECT system.

MATERIALS AND METHODS

Detection system description

The gamma camera consists of a 22 × 22 pixellated scintillator array of 1.8 mm × 1.8 mm × 5 mm NaI(Tl) crystals with 0.2-mm white epoxy gap of diffuse, opaque reflective material between the crystals (Fig. 1 (a)) optically coupled to a 2″ flat PSPMT (Hamamatsu H8500)

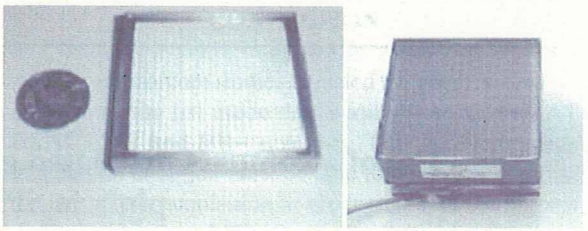

a b

Fig. 1 (a) Photograph of pixellated NaI scintillator array. (b) Photograph of 2-inch flat panel position-sensitive photomultiplier tube.

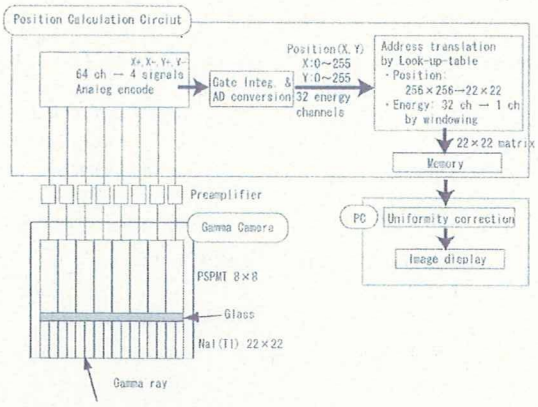

Fig. 2 Schematic diagram of position calculation circuit.

with 64 channel anodes (Fig. 1 (b)). The scintillator array has a 0.5-mm aluminum window and 2-mm glass window on gamma-ray input and light output sides, respectively. The active imaging region of the camera was 43.8 mm × 43.8 mm square.

Figure 2 shows a schematic diagram of a position calculation circuit. Analog outputs from 64 PSPMTs through preamplifiers are weighted in proportion to coordinates and are summed in X+, X–, Y+ and Y– directions. After applying gated integration and analog-to-digital conversion for these encoded four analog outputs, the position is obtained by calculating the center of the gravity from the four signals, and is assigned to either pixel in 256 × 256 matrix as a raw image. Also an energy spectrum with 32 channels is collected for each pixel. And then, by address translation using look-up-table (LUT), the raw image of 256 × 256 × 32 matrix is converted to 22 × 22 × 1 image matrix according to the number of scintillators and energy window described below. The counts within the region divided by 22 × 22-matrix grid are summed. The positions of horizontal and vertical lines of the grid are alterable by the interactive tool (Fig. 3) on a personal computer (Windows 2000 (Microsoft)) (PC). Thus, all events are assigned to a 1.8 mm × 1.8 mm crystal in the image matrix. On the other hand, the energy window is set as above and below channel widths from a photopeak

channel searched in each pixel. We assume the use of two radioisotopes of ^{99m}Tc and ^{201}Tl. The main photopeaks are 140 keV and 70 keV for ^{99m}Tc and ^{201}Tl, respectively. Here, the camera gain for ^{201}Tl was set about twice as much as that for ^{99m}Tc. The energy width with each channel corresponds to approximately 10 keV and 5 keV for ^{99m}Tc and ^{201}Tl, respectively. The energy window was actually set at five channels, namely, approximately 36% for both ^{99m}Tc and ^{201}Tl and centered on the photopeak channel searched. Finally, the converted 22 × 22-pixel image is stored on memory and then is transferred to the PC. The PC can perform several tasks such as correcting uniformity, displaying and analyzing images. Figure 3 shows flood raw image by irradiating with a ^{99m}Tc point source. Separation between pixels was well performed except for pixels in columns and rows at the edge. The effective image field-of-view (FOV) that does not enclose the edge pixels was 20 × 20 pixels (or 39.8 mm × 39.8 mm). The resulting image is used as correction matrix to correct for non-uniformity in sensitivity over camera's FOV.

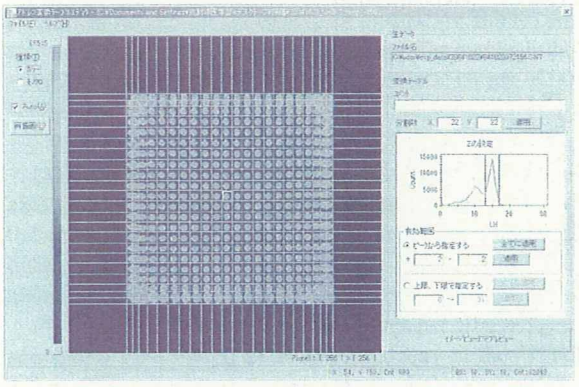

Fig. 3 Interactive tool on PC for making address translation table. The flood raw image was obtained by irradiating with a ^{99m}Tc point source. The separation between pixels was well performed.

Collimator design

As shown in Figures 4 (a) and (b), the pinhole collimator made of tungsten is attached on the gamma camera and has a 0.5-mm or 1.0-mm aperture, 60° opening angle and 39.57-mm focal length. The collimator has a flat face of the single knife-edge pinhole, in order to achieve higher sensitivity and spatial resolution (larger magnification factor) by positioning the pinhole closer to the object. The camera is shielded by tungsten to avoid the penetration of the photon from the surrounding area.

Projection image acquired with the pinhole collimator has non-uniform sensitivity distribution due to the pinhole geometry.[24,25] This non-uniformity can be corrected by using a correction matrix derived from a flood source contained in a thin plate. Figure 4 (c) shows a projection image obtained from the flood source. The correction matrix from this projection image, which has high counts around the center and low counts at the periphery, was actually used to correct the non-uniformity of pinhole sensitivity.

SPECT FOV, namely, the diameter of reconstruction sphere is expressed as:

$$FOV = 2b \sin\left(\frac{\alpha}{2}\right), \tag{1}$$

where b is the distance from the pinhole to the rotation center of the object (radius of rotation: ROR), α is the opening angle of the pinhole collimator. However, when the diameter of the effective image region of camera c_e is shorter than the diameter of the collimator base c, SPECT FOV_e (effective FOV) is expressed as:

$$FOV_e = \frac{c_e}{c} FOV. \tag{2}$$

In this collimator c_e of 39.8 mm is shorter than c of 45.69 mm. Therefore, when b is 30 mm, FOV_e becomes 26.1 mm.

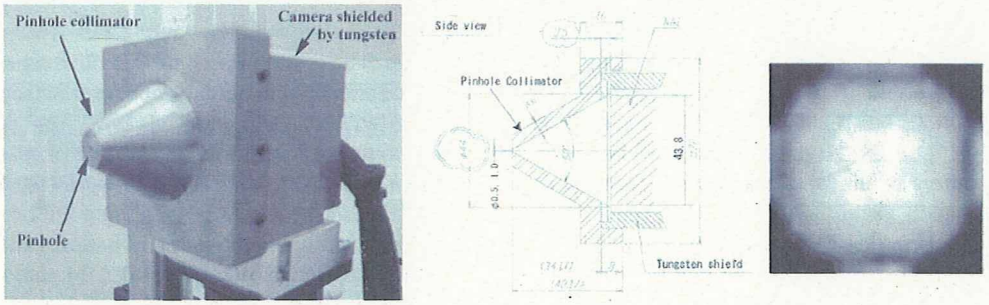

a b c

Fig. 4 (a) Photograph of the pinhole collimator attached to the compact gamma camera. (b) Drawing of side view of the pinhole collimator. (c) Sensitivity map of pinhole collimator. This map was obtained from a flood source filled in a thin plate parallel to the detector and was used to correct non-uniformity of pinhole sensitivity.

SPECT imaging system

Figure 5 shows the pinhole SPECT acquisition system using a compact gamma camera. Data acquisition is controlled by the PC through the camera controller. The rotation of the object stage is synchronized to step and shoot acquisition of the SPECT camera.

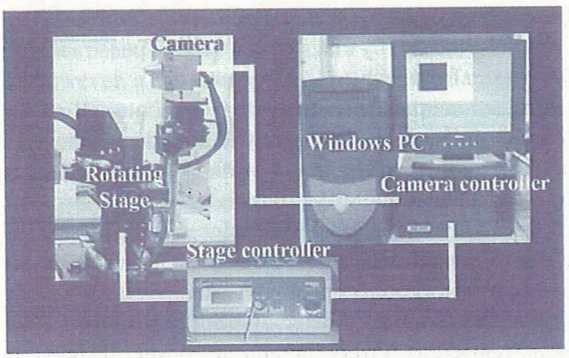

Fig. 5 Pinhole SPECT acquisition system using compact gamma camera. This system consists of compact gamma camera with pinhole collimator, camera controller, PC, object rotating stage and stage controller.

Basic system performances

The performances of the detection system such as the energy resolution, system spatial resolution, sensitivity and linearity of the count rate were examined with ^{99m}Tc (140 keV) and ^{201}Tl (70 keV) sources.

(1) Energy resolution: Energy resolution was measured by uniform irradiation with a 2.18 MBq ^{99m}Tc point source placed at 2 m distant from the camera,without the collimator for 12 hours and is defined for each crystal's energy spectrum as full width at half maximum (FWHM) of the photopeak divided by its amplitude. The energy resolution was obtained from an energy spectrum for one crystal near the center of the camera.

(2) System spatial resolution: The FWHMs of the line spread functions (LSFs) were measured in planar image using ^{99m}Tc and ^{201}Tl line sources with 1.14-mm inner diameter placed at 30 mm distant from the 1-mm pinhole. The magnification factor was 1.32. The LSFs of line sources were computed by deconvoluting with rectangular function of 1.14-mm width. The spatial resolutions were defined as the FWHM of Gaussian function obtained from this deconvolution.

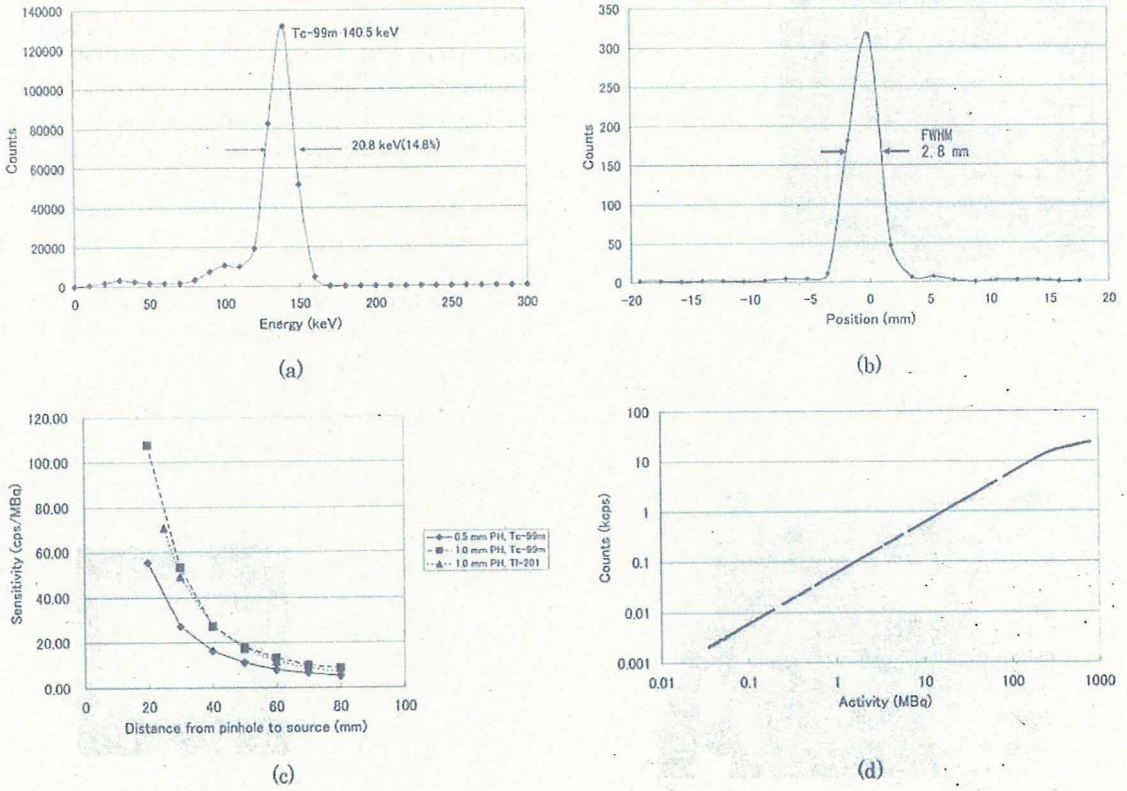

Fig. 6 (a) Energy spectrum obtained from this detection system. The energy resolution was 14.8% FWHM at 140 keV. (b) Planar image profile of 1.14-mm ^{99m}Tc line source. The system spatial resolution obtained from the LSF was 2.8-mm FWHM. (c) On-axis sensitivities for ^{99m}Tc or ^{201}Tl as a function of distance from the pinhole for 0.5-mm or 1.0-mm diameters. (d) Relationship between the source activity and the count rate measured by following decay of ^{99m}Tc source.

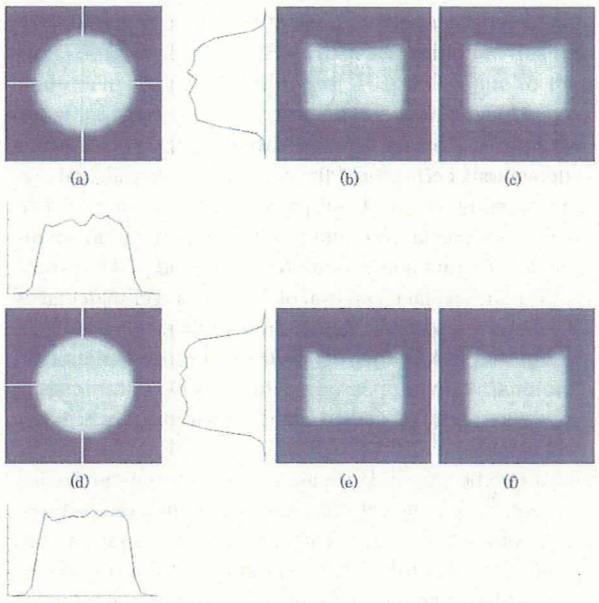

Fig. 7 SPECT images of uniform cylindrical phantom. (a)–(c) are without pinhole sensitivity correction. (d)–(f) are with the correction. (a) and (d) are transverse images. (b) and (e) are coronal images. (c) and (f) are sagittal images. The profiles in the *x* and *y* directions were attached to the transverse images of (a) and (d).

(3) Sensitivity: The system sensitivity on the central axis was measured using a small cylindrical phantom of 0.1 m*l* at eight points in the range from 20 to 80-mm distances with 0.5- or 1.0-mm pinholes and ^{99m}Tc or ^{201}Tl sources.

(4) Linearity of count rate: The counts per 10 min were sequentially measured by following decay of the ^{99m}Tc source. The cylindrical phantom made of glass with 24.3-mm outer diameter and 21.8-mm inner diameter was filled with uniform ^{99m}Tc solution. The center of the phantom was positioned at 30 mm distant from the 1-mm pinhole. Consequently, the relationship between activity and detected counts was examined.

Flood phantom SPECT study

A flood phantom SPECT study was performed to evaluate the uniformity of the reconstruction images. The phantom used in this study was the same one as the cylindrical phantom used to evaluate the linearity of count rate, and was filled with uniform ^{99m}Tc solution. The pinhole collimator with 1-mm diameter was used. The ROR was 30 mm. This resulted in a magnification factor of 1.32. Projection data of 120 views were acquired over 360° using step and shoot acquisition; 10 sec/step, 3° increments. Decay correction and the above-mentioned pinhole sensitivity correction were applied for projection data before reconstruction. The projection data were reconstructed using our previously validated pinhole 3D-OSEM method employing a 3D voxel-driven projector in both back- and forward-projections with eight subsets and two iterations. The corrections for attenuation, scatter and penetration were not done.

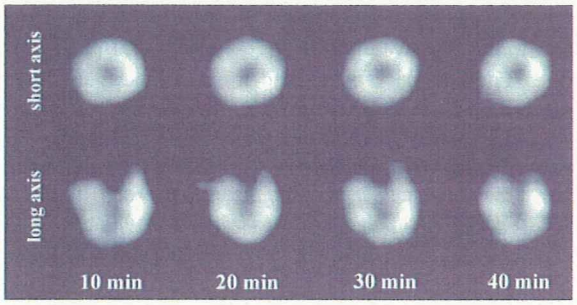

Fig. 8 Short- and long-axial images of rat myocardial perfusion obtained by sequential SPECT scans. The left ventricular walls and cavities were clearly visible in all of four frames obtained for 40 min.

Animal SPECT study

Rat myocardial perfusion SPECT scans were sequentially performed. A male rat weighing 220 g was anesthetized with sodium pentobarbital and held vertically on the object rotating stage, and then was scanned after intravenous 2-min administration of 6.21 MBq/1.5 m*l* ^{201}TlCl into the tail vein. The pinhole of 1 mm was used. The ROR was 30 mm. Scans for 10 min were sequentially performed four times using 360° step and shoot acquisition; 5 sec/step, 3° increments. Like the flood phantom study, projection data were reconstructed using our pinhole 3D-OSEM method with eight subsets and two iterations. Corrections for attenuation, scatter, penetration and pinhole sensitivity were not performed.

RESULTS

Basic system performances

(1) Energy resolution: Figure 6 (a) shows a sample energy spectrum from one crystal near the center of the detector block. The energy resolution was 20.8-keV (14.8%) FWHM at 140 keV.

(2) System spatial resolution: Figure 6 (b) shows a planar image profile of the ^{99m}Tc line source. The spatial resolutions were 2.8-mm FWHM and 2.5-mm FWHM for ^{99m}Tc and ^{201}Tl, respectively.

(3) Sensitivity: Figure 6 (c) shows system sensitivity on the central axis as a function of distance from the pinhole for ^{99m}Tc with 0.5- and 1.0-mm pinholes and for ^{201}Tl with 1.0-mm pinhole. The sensitivity of ^{201}Tl was slightly smaller than that of ^{99m}Tc. In the case of ^{99m}Tc, the sensitivities at a pinhole-source distance of 30 mm were 27.0 and 53.0 cps/MBq with 0.5-mm and 1.0-mm pinholes, respectively. In the case of ^{201}Tl, the sensitivity at the same distance was 49.1 cps/MBq with the 1.0-mm pinhole.

(4) Linearity of count rate: Figure 6 (d) shows the relationship between the source activity and the count rate. The linearity was good up to 10 kcps and the regression line was $y = 0.0588x + 0.009$ ($r^2 = 0.9999$). However, the ratio of the count rate to the source activity gradually decreased over 10 kcps.

Flood phantom SPECT study

Figure 7 shows SPECT images of uniform cylindrical phantom. The image reconstructed with pinhole geometrical sensitivity correction was almost uniform, while the image without the correction had high counts around the center and low counts at the periphery.

Animal SPECT study

Figure 8 shows sequential SPECT images of a rat myocardial perfusion in four frames obtained for 40 min. The left ventricular walls and cavities were clearly visible in all frames.

DISCUSSION

We have developed a compact SPECT system using a compact pixellated gamma camera for small animals and succeeded in sequential SPECT imaging of rat myocardial perfusion. In this system we employed 2″ PSPMT rather than 5″ PSPMT which was used by other investigators[21–23] because the use of 2″ PSPMT allows one to construct a more inexpensive, compact and lighter system.

The energy resolution of 14.8% FWHM in this camera was worse than that of approximately 10% FWHM in clinical SPECT gamma camera. So, the profile of the photopeak in the energy spectrum was as broad as the 36% energy window used. McElroy et al. reported[22] that in their pinhole system, scatter fraction did not contribute a significant amount to images (about 5%) for mouse sized 2.5-cm diameter cylinder when the usual 20% energy window was used in their system with a 11.4% energy resolution. However, the scatter fractions were about 15% and 20% for rat sized 3.8-cm and 5.05-cm diameter cylinders. Further study is needed to evaluate the contribution of scatter photons and develop proper scatter correction technique[26] for our system.

The measured system spatial resolutions were 2.8-mm FWHM and 2.5-mm FWHM for ^{99m}Tc and ^{201}Tl, respectively. Here, the theoretical system spatial resolution for a pinhole collimated gamma camera R_0 is given by

$$R_0 \cong \sqrt{\left(\frac{b}{f}R_i\right)^2 + \left(d_e\frac{f+b}{f}\right)^2}, \quad (3)$$

where f is the distance between the pinhole and the detector (focal length), b is ROR, R_i is the intrinsic camera resolution, and d_e is the effective pinhole diameter expressed as:

$$d_e \approx \sqrt{d\left[d + \frac{2}{\mu}\tan\left(\frac{\alpha}{2}\right)\right]}, \quad (4)$$

where d is the actual pinhole diameter, μ is the linear attenuation coefficient of the collimator material, and α is the opening angle of the pinhole collimator.[22,27] The theoretical spatial resolutions in this experimental condition are 2.5 mm and 2.3 mm for ^{99m}Tc and ^{201}Tl, respectively. The spatial resolution of ^{99m}Tc is larger than that of ^{201}Tl due to its higher energy ($\mu \approx 4.098$ mm^{-1} for ^{99m}Tc and $\mu \approx 20.870$ mm^{-1} for ^{201}Tl) and more penetration photons, which appeared in the experimental results. However, the measured spatial resolutions are slightly worse than the theoretical ones. As one of the reasons for the difference, the theoretical calculation assumes a double knife-edge pinhole collimator, while our pinhole collimator is single knife-edge. The number of penetration photons in single knife-edge is larger than that in double knife-edge. Therefore, the actual pinhole diameter for single knife-edge is larger than that for double knife-edge. By accounting for the difference of the knife-edge of the collimator, the measured spatial resolutions largely agree with the theoretical ones. Weber et al. obtained rat myocardial images at a spatial resolution of 2.8-mm FWHM.[11] The spatial resolution measured in our system is almost equal to that measured in their system.

However, the spatial resolution obtained in our system might be unsatisfactory for mouse imaging. Resolution can be improved by using a smaller diameter pinhole, but this will decrease sensitivity in return for improvement of resolution. Decreasing the crystal size or enlarging the detection area of the camera can improve resolution without decreasing sensitivity. Resolution is usually degraded by non-zero diameter and edge penetration of a pinhole. Alternatively, this degraded resolution can be recovered by incorporating the realistic pinhole model into reconstruction software.[28,29] This approach does not require any modification of hardware and is applicable to our system.

From Figure 6 (c), positioning the pinhole closer to the object is important for improvement of sensitivity in pinhole SPECT. In that respect, the flat face of a single-knife edge collimator is advantageous. However, care must be taken of the effect of penetration for thin, single knife-edge collimator. The sensitivity of ^{201}Tl was slightly smaller than that of ^{99m}Tc. This is considered that the number of penetrations for ^{201}Tl was less than that for ^{99m}Tc due to lower energy of ^{201}Tl compared to ^{99m}Tc. In future we need to evaluate the effect of the penetration for both ^{99m}Tc and ^{201}Tl in single-knife edge.

A good linearity of the count rate up to 10 kcps was shown in this study, although the ratio of the count rate to the source activity gradually decreased over 10 kcps. This characteristic of the count rate allows the present compact gamma camera system to be applied for rat myocardial

SPECT imaging with ^{201}Tl because the mean count rate was 0.52 kcps during SPECT data acquisition in this rat study. This upper limitation of 10 kcps is due to the transfer speed of the electric circuit which can be improved by replacement with faster electronics. The present system also produced homogeneous reconstructed images of the cylindrical phantom as shown in Figure 7. The homogeneity of images reconstructed from the flood phantom is important for quantitative analysis of physiological function.

In the animal SPECT study, rat myocardial tomographic images were sequentially obtained. The SPECT images could clearly visualize the rat myocardium and cardiac cavity. It is anticipated that these images could be significantly improved if image gate is employed. The time-dependent change of regional tissue radioactivity concentration obtained from such sequential tomographic images can be applied for kinetic analysis using a compartment model to estimate the regional myocardial blood flow.[30] The results for phantom and animal studies support the feasibility of our system for quantitative assessments of regional myocardial blood flow on rat. Further study is needed to quantify myocardial blood flow by pinhole SPECT. Deloar et al. suggested that physical factors such as penetration and scatter are considered.[31] Also, Wang et al. reported that both of attenuation correction (AC) and scatter compensation (SC) are important to improve quantitative accuracy because the values of reconstructed images were underestimated by 15% without AC and overestimated by 9% with only AC, while the quantitative accuracy was below 3% with both AC and SC.[32]

If this compact camera is combined with a rotating apparatus, the camera will rotate around the animal laid down. So, we can observe physiological function of small animals in more natural conditions, against especially acquiring complete data set with two orbits,[18] than when the animals are held vertically like in this study. The misalignment of a center of rotation (COR) might be a problem, if the camera is rotated. It causes serious artifacts in the reconstructed image.[13] However, our compact camera is sufficiently light to avoid the misalignment of the COR compared to clinical gamma camera. In the near future, we will construct a small animal pinhole SPECT system, which permits acquisition of complete data by two-circular orbit, using a compact gamma camera.

CONCLUSION

We have developed a compact SPECT system using a compact pixellated gamma camera for small animals. The camera with an active detection area of 43.8 mm × 43.8 mm was equipped with a pinhole collimator. We evaluated the basic physical performances and succeeded in sequential SPECT imaging of rat myocardial perfusion. The present system may be of use for quantitation of biological functions such as myocardial blood flow in small animals.

ACKNOWLEDGMENT

This study was financially supported by the Budget for Nuclear Research of the Ministry of Education, Culture, Sports, Science and Technology, based on screening and counseling by the Atomic Energy Commission, Japan.

REFERENCES

1. Meikle SR, Eberl S, Iida H. Instrumentation and methodology for quantitative pre-clinical imaging studies. *Curr Pharm Des* 2001; 7 (18): 1945–1966.
2. Chatziioannou AF. PET scanners dedicated to molecular imaging of small animal models. *Mol Imaging Biol* 2002; 4 (1): 47–63.
3. Hirai T, Nohara R, Ogoh S, Chen LG, Kataoka K, Li XH, et al. Serial evaluation of fatty acid metabolism in rats with myocardial infarction by pinhole SPECT. *J Nucl Cardiol* 2001; 8 (4): 472–481.
4. Scherfler C, Donnemiller E, Schocke M, Dierkes K, Decristoforo C, Oberladstätter M, et al. Evaluation of striatal dopamine transporter function in rats by *in vivo* β-[^{123}I]CIT pinhole SPECT. *NeuroImage* 2002; 17: 128–141.
5. Acton PD, Choi SR, Plössl K, Kung HF. Quantification of dopamine transporters in the mouse brain using ultra-high resolution single-photon emission tomography. *Eur J Nucl Med* 2002; 29 (5): 691–698.
6. Aoi T, Watabe H, Deloar HM, Ogawa M, Teramoto N, Kudomi N, et al. Absolute quantitation of regional myocardial blood flow of rats using dynamic pinhole SPECT. In Conference Record of 2002 IEEE Nuclear Science Symposium and Medical Imaging Conference (CD-ROM), 2003: M11-185.
7. Jeavons AP, Chandler RA, Dettmar CAR. A 3D HIDAC-PET camera with sub-millimetre resolution for imaging small animals. *IEEE Trans Nucl Sci* 1999; 46 (3): 468–473.
8. Seidel J, Vaquero JJ, Green MV. Resolution uniformity and sensitivity of the NIH ATLAS small animal PET scanner: comparison to simulated LSO scanners without depth-of-interaction capability. *IEEE Trans Nucl Sci* 2003; 50 (5): 1347–1350.
9. Tai YC, Chatziioannou AF, Yang Y, Silverman RW, Meadors K, Siegel S, et al. MicroPET II: design, development and initial performance of an improved microPET scanner for small-animal imaging. *Phys Med Biol* 2003; 48: 1519–1537.
10. Jaszczak RJ, Li J, Wang H, Zalutsky MR, Coleman RE. Pinhole collimation for ultra-high-resolution, small-field-of-view SPECT. *Phys Med Biol* 1994; 39: 425–437.
11. Weber DA, Ivanovic M, Franceschi D, Strand SE, Erlandsson K, Franceschi M, et al. Pinhole SPECT: an approach to *in vivo* high resolution SPECT imaging in small laboratory animals. *J Nucl Med* 1994; 35 (2): 342–348.
12. Ishizu K, Mukai T, Yonekura Y, Pagani M, Fujita T, Magata Y, et al. Ultra-high resolution SPECT system using four pinhole collimators for small animal studies. *J Nucl Med* 1995; 36 (12): 2282–2287.

13. Ogawa K, Kawade T, Nakamura K, Kubo A, Ichihara T. Ultra high resolution pinhole SPECT for small animal study. *IEEE Trans Nucl Sci* 1998; 45 (6): 3122–3126.
14. Moore SC, Zimmerman RE, Mahmood A, Mellen R, Lim CB. A triple-detector, multiple-pinhole system for SPECT imaging rodents. [Abstract] *J Nucl Med* 2004; 45 (suppl): 97–98.
15. Beekman FJ, van der Have F, Vastenhouw B, van der Linden AJ, van Rijk PP, Burbach JP, et al. U-SPECT-I: a novel system for submillimeter-resolution tomography with radiolabeled molecules in mice. *J Nucl Med* 2005; 46 (7): 1194–1200.
16. Sun M, Izaguirre EW, Funk T, Hwang AB, Carver J, Thompson S, et al. A CdZnTe-based high-resolution microSPECT system. [Abstract] *J Nucl Med* 2005; 46 (suppl 2): p170.
17. Lackas C, Hoppin JW, Schramm NU. Performance analysis of a submillimeter-resolution multi-pinhole SPECT small-animal imaging system. [Abstract] *J Nucl Med* 2005; 46 (suppl 2): p171.
18. Zeniya T, Watabe H, Aoi T, Kim KM, Teramoto N, Hayashi T, et al. A new reconstruction strategy for image improvement in pinhole SPECT. *Eur J Nucl Med Mol Imaging* 2004; 31 (8): 1166–1172.
19. Liu Z, Kastis GA, Stevenson GD, Barrett HH, Furenlid LR, Kupinski MA, et al. Quantitative analysis of acute myocardial infarct in rat hearts with ischemia-reperfusion using a high-resolution stationary SPECT system. *J Nucl Med* 2002; 43 (7): 933–939.
20. Schramm NU, Ebel G, Engeland U, Schurrat T, Béhé M, Behr TM. High-resolution SPECT using multipinhole collimation. *IEEE Trans Nucl Sci* 2003; 50 (3): 315–320.
21. Schramm N, Wirrwar A, Sonnenberg F, Halling H. Compact high resolution detector for small animal SPECT. *IEEE Trans Nucl Sci* 2000; 47 (3): 1163–1167.
22. McElroy DP, MacDonald LR, Beekman FJ, Wang Y, Patt BE, Iwanczyk JS, et al. Performance evaluation of A-SPECT: a high resolution desktop pinhole SPECT system for imaging small animals. *IEEE Trans Nucl Sci* 2002; 49 (5): 2139–2147.
23. Wojcik R, Goode AR, Smith MF, Beller GA, Ellman PI, Majewski S, et al. Dedicated small field of view SPECT system based on a 5″ PSPMT and crystal scintillator array for high resolution small animal cardiac imaging. In Conference Record of 2003 IEEE Nuclear Science Symposium and Medical Imaging Conference (CD-ROM), 2004: M3-43.
24. Smith MF, Jaszczak RJ. The effect of gamma ray penetration on angle-dependent sensitivity for pinhole collimation in nuclear medicine. *Med Phys* 1997; 24 (11): 1701–1709.
25. Metzler SD, Bowsher JE, Smith MF, Jaszczak RJ. Analytical determination of pinhole collimator sensitivity with penetration. *IEEE Trans Med Imag* 2001; 20 (8): 730–741.
26. Deloar HM, Watabe H, Kim KM, Aoi T, Kunieda E, Fujii H, et al. Optimization of the width of the photopeak energy window in the TDCS technique for scatter correction in quantitative SPECT. *IEEE Trans Nucl Sci* 2004; 51 (3): 625–630.
27. Anger HO. Radioisotope cameras. In: *Instrumentation in nuclear medicine*, Hine GJ (ed), New York; Academic, 1967: 485–552.
28. Bequé D, Vanhove C, Andreyev A, Nuyts J, Defrise M. Correction for impact camera motion and resolution recovery in pinhole SPECT. In Conference Record of 2004 IEEE Nuclear Science Symposium and Medical Imaging Conference (CD-ROM), 2005: M2-173.
29. Cao Z, Bal G, Acton PD. Pinhole SPECT reconstruction with resolution recovery. [Abstract] *J Nucl Med* 2005; 45 (suppl 2): 109–110.
30. Iida H, Eberl S. Quantitative assessment of regional myocardial blood flow with thallium-201 and SPECT. *J Nucl Cardiol* 1998; 5: 313–331.

Human Molecular Genetics, 2006, Vol. 15, No. 20 *3024–3033*
doi:10.1093/hmg/ddl244
Advance Access published on September 7, 2006

Impact of the DISC1 Ser704Cys polymorphism on risk for major depression, brain morphology and ERK signaling

Ryota Hashimoto[1,2,3,*,†], Tadahiro Numakawa[3,†], Takashi Ohnishi[3,4,†], Emi Kumamaru[3], Yuki Yagasaki[3], Tetsuya Ishimoto[5], Takeyuki Mori[3,4], Kiyotaka Nemoto[4], Naoki Adachi[3], Aiko Izumi[3], Sachie Chiba[2,6], Hiroko Noguchi[3], Tatsuyo Suzuki[7], Nakao Iwata[7], Norio Ozaki[8], Takahisa Taguchi[5], Atsushi Kamiya[9], Asako Kosuga[10], Masahiko Tatsumi[10], Kunitoshi Kamijima[10], Daniel R. Weinberger[11], Akira Sawa[12,13] and Hiroshi Kunugi[3]

[1]The Osaka-Hamamatsu Joint Research Center For Child Mental Development and [2]Department of Psychiatry, Osaka University Graduate School of Medicine, D3, 2-2 Yamadaoka, 4-1-1 Suita, Osaka 565-0871, Japan, [3]Department of Mental Disorder Research, National Institute of Neuroscience, National Center of Neurology and Psychiatry, Kodaira, Tokyo, Japan, [4]Department of Radiology, National Center Hospital of Mental, Nervous, and Muscular Disorders, National Center of Neurology and Psychiatry, Kodaira, Tokyo, Japan, [5]Neuronics R.G. Special Division for Human Life Technology, National Institute of Advanced Industrial Science and Technology, Ikeda, Osaka, Japan, [6]Department of Biotechnology and Life Science, Tokyo University of Agriculture and Technology, Koganei, Tokyo, Japan, [7]Department of Psychiatry, Fujita Health University School of Medicine, Toyoake, Aichi, Japan, [8]Department of Psychiatry, Nagoya University Graduate School of Medicine, Nagoya, Aichi, Japan, [9]Department Psychiatry, Johns Hopkins University, Baltimore, MD, USA, [10]Department of Psychiatry, Showa University School of Medicine, Tokyo, Japan, [11]Genes, Cognition and Psychosis Program, Clinical Brain Disorders Branch, National Institute of Mental Health, National Institutes of Health, Bethesda, MD, USA and [12]Department of Psychiatry and [13]Department of Neuroscience, Program in Cellular Molecular Medicine, Johns Hopkins University School of Medicine, Baltimore, MD, USA

Received May 22, 2006; Revised August 8, 2006; Accepted September 4, 2006

Disrupted-in-schizophrenia 1 (DISC1), identified in a pedigree with a familial psychosis with the chromosome translocation (1:11), is a putative susceptibility gene for psychoses such as schizophrenia and bipolar disorder. Although there are a number of patients with major depressive disorder (MDD) in the family members with the chromosome translocation, the possible association with MDD has not yet been studied. We therefore performed an association study of the DISC1 gene with MDD and schizophrenia. We found that Cys704 allele of the Ser704Cys single-nucleotide polymorphism (SNP) was associated with an increased risk of developing MDD ($P = 0.005$, odds ratio = 1.46) and stronger evidence for association in a multi-marker haplotype analysis containing this SNP ($P = 0.002$). We also explored possible impact of Ser704Cys on brain morphology in healthy volunteers using MR imaging. We found a reduction in gray matter volume in cingulate cortex and a decreased fractional anisotropy in prefrontal white matter of individuals carrying the Cys704 allele compared with Ser/Ser704 subjects. In primary neuronal culture, knockdown of endogenous DISC1 protein by small interfering RNA resulted in the suppression of phosphorylation of ERK and Akt, whose signaling pathways are implicated in MDD. When effects of sDISC1 (Ser704) and cDISC1 (Cys704) proteins were examined separately, phosphorylation of ERK was greater in sDISC1 compared with cDISC1. A possible biological mechanism of MDD might be implicated by these convergent data that Cys704 DISC1 is associated with the lower biological activity on ERK signaling, reduced brain gray matter volume and an increased risk for MDD.

*To whom correspondence should be addressed. Tel: +81 668793074; Fax: +81 668793059; Email: hashimor@psy.med.osaka-u.ac.jp
†The authors wish it to be known that, in their opinion, the first three authors should be regarded as joint First Authors.

INTRODUCTION

The disrupted-in-schizophrenia 1 (DISC1) gene was initially identified at the breakpoint of a balanced translocation (1,11)(q42.1;q14.3), which segregated with major mental disorders in a large Scottish family (1). In this family, patients with schizophrenia, bipolar disorder and recurrent major depressive disorder (MDD) had been identified as carriers of the translocation (1,2). Subsequent genetic studies in several independent populations, including association and linkage studies, have also suggested that the DISC1 gene may be implicated in both schizophrenia and bipolar disorder (3–10). Previous studies suggest that genetic variations within the DISC1 gene, which increase risk for schizophrenia, are associated with the cerebral cortical gray matter and hippocampal volumes and function (9,11,12). However, no association study between the DISC1 gene and MDD has not yet been reported, despite there are more patients with MDD than those with schizophrenia in the original Scottish family members with translocation.

DISC1 is a multi-functional protein. Several research groups have identified DISC1 interacting proteins, which are associated with the components of the cytoskeleton and centrosome, such as dynein, Nudel, elongation protein zeta-1, etc. (13–18). DISC1 plays critical roles on the cerebral cortex development via microtubular dynamics and the DISC1–dynein complex (13). Another function of DISC1 may be modulation of cAMP signaling via an interaction with phosphodiesterase 4B, which also has been found to be disrupted by a balanced translocation in a patient with schizophrenia (19). Other functions of DISC1, including the mitochondrial and nuclear related functions, have also been suggested (15,20,21).

Here, we report an association of the genetic variations of DISC1, including Ser704Cys (rs821616) single-nucleotide polymorphism (SNP) and MDD. The risk allele (Cys704) for MDD is associated with the reduced gray matter volume and fractional anisotropy (FA) in prefrontal white matter in healthy subjects. Furthermore, the risk allele is linked to lower ERK activity (extracellular signal-regulated kinase), which has been suggested to have a role in the pathophysiology in MDD.

RESULTS

Association between the genetic variants of the DISC1 gene and major depression

We examined possible association between genetic variants in the DISC1 gene, including Ser704Cys SNP and MDD or schizophrenia. We genotyped 13 SNPs to cover the DISC1 locus at an average density of 31 kb. We found a significant association between genetic variations in DISC1 and MDD (Table 1). The Cys allele frequency of SNP12 (Ser704Cys) was greater in patients with MDD when compared with controls ($\chi^2 = 7.88$, df = 1, $P = 0.005$, odds ratio = 1.46, 95% CI 1.12–1.92). There was a weak evidence for an association with SNP1 ($P = 0.048$). As previous association studies of the DISC1 gene applied three-marker haplotype analysis (4,8,9), we performed this analysis. Consistent with the individual marker results, the three marker haplotypes containing SNPs 11–13 were associated with MDD: SNP11 (G allele)–SNP12(Cys)–SNP13(C allele) ($P = 0.002$; Table 2). When we examined the association between genetic variations of DISC1 and schizophrenia, a weak evidence for association was observed with SNP7 ($P = 0.0496$), whereas SNP12 (Ser704Cys) was not significantly associated with schizophrenia (Table 1). Because a prior study reported sex-dependent effects on association with schizophrenia (4), we examined males and females separately. This analysis revealed stronger evidence for association with SNP9 in female patients with schizophrenia ($P = 0.0088$), but no association in male subjects, whereas a prominent gender effect was not found in MDD (Table 3). Three marker haplotypes were not associated with schizophrenia (data not shown). SNP12 showed a strong linkage disequilibrium (LD) with SNP10 and SNP11, moderate LD with SNP1 and SNP13 and weak LD with SNP6 in controls, and similar LD results were obtained in MDD and schizophrenia (Supplementary Material, Tables S1–S3). LD pattern of our data was similar to that of HapMap database in the Japanese population. Our results suggest that DISC1 is associated with MDD and with schizophrenia and that Ser704Cys SNP, in particular, is associated with MDD in our sample.

Effects of the DISC1 Ser704Cys polymorphism on *in vivo* brain structure

As the abnormalities in the brain gray matter volume and white matter microstructure have been implicated in the biology of mood disorders and schizophrenia (22,23), we examined the possible effects of the Ser704Cys SNPs and other associated SNPs with schizophrenia on brain structure in healthy subjects (demographic information for Ser704Cys, Table 4). We found a bilateral (left dominant) reduction in the gray matter volume in the anterior cingulate cortex (ACC) [Brodmann area (BA) 24, Talairach coordinates x, y, $z = -6$, 27, 17, respectively, $t = 3.58$], cingulate gyrus (BA24, Talairach coordinates x, y, $z = 0$, 3, 34, respectively, $t = 3.7$) and the posterior cingulate gyrus (BA31, Talairach coordinates x, y, $z = -9$, -39, 36, respectively, $t = 3.39$) in cys-DISC1 carriers (cys/cys and cys/ser) compared with ser/ser-DISC1 individuals by tensor-based morphometry (TBM) analysis (Fig. 1, upper panel). When we analyzed the effect of this SNP on brain morphology in the other direction (i.e. cys > ser), we found a significant reduction in the volumes of the lateral ventricle, interhemispheric fissure and the bilateral Sylvian fissure in ser/ser-DISC1 individuals compared with cys-DISC1 carriers (Fig. 1, lower panel). This finding suggests that cys-DISC1 carriers have expanded cerebrospinal fluid (CSF) space compared with ser/ser-DISC1 individuals, possibly consistent with our finding that cys carriers in our analysis have reductions in tissue volume measures. We did not detect significant differences in hippocampal volume related to this DISC1 polymorphism with even at a lenient threshold at $P < 0.05$. In comparison with ser/ser-DISC1 individuals, cys-DISC1 carriers demonstrated a significantly decreased FA value in the frontal white matter ($P < 0.001$) (Fig. 2). The reversed contrast, i.e. increased FA in cys-DISC1 carriers, was not observed even at the level of

Table 1. Allele distributions for 13 SNPs in the DISC1 gene in patients with MDD, those with schizophrenia and controls

SNP	dbSNP	Distance from SNP1	Major/minor polymorphism	Amino acid substitution	Controls $n = 717$	MDD $n = 373$	*P*-value	OR	SZ $n = 658$	*P*-value	OR
1	rs6541281		C/T		0.122	0.094	*0.048*	*0.75*	0.105	0.16	—
2	rs3738401	17161	G/A	Gln264Arg	0.260	0.263	0.89	—	0.264	0.83	—
3	rs1340982	48898	C/T		0.461	0.456	0.82	—	0.459	0.92	—
4	rs1322784	115801	T/C		0.351	0.371	0.36	—	0.375	0.19	—
5	rs1535529	141475	C/T		0.425	0.441	0.48	—	0.410	0.42	—
6	rs7551537	159083	C/T		0.363	0.363	0.98	—	0.382	0.29	—
7	rs999710	197809	C/T		0.404	0.424	0.39	—	0.441	*0.05*	1.16
8	rs967433	218681	T/C		0.409	0.416	0.76	—	0.387	0.24	—
9	rs821577	253923	G/T		0.201	0.166	0.05	—	0.172	0.06	—
10	rs821597	289130	T/C		0.414	0.438	0.28	—	0.404	0.60	—
11	rs843979	317474	C/G		0.335	0.358	0.29	—	0.334	0.92	—
12	rs821616	331464	A/T	Ser704Cys	0.104	0.145	*0.005*	*1.46*	0.122	0.14	—
13	rs2806465	353160	G/C		0.376	0.378	0.92	—	0.370	0.75	—

Minor allele frequencies in controls are shown. SZ, schizophrenia, OR, odds ratio. Significant results ($P < 0.05$) indicated by italics.

Table 2. Three-marker haplotype analysis among patients with major depression and controls

SNP	Haplotype										
1	2										
2	1	1									
3	1	1	2								
4		2	1	1							
5			2	1	1						
6				2	2	2					
7					1	1	1				
8						2	2	1			
9							2	2	2		
10								1	2	2	
11									1	2	2
12										2	2
13											2
Global *P*-value	*0.030*	0.19	*0.043*	0.81	0.74	0.55	0.69	0.20	*0.012*	0.17	0.057
Individual *P*-value	*0.017*	*0.026*	*0.018*	0.24	0.25	0.25	0.19	*0.023*	*0.019*	*0.017*	*0.002*
Haplotype frequency in control	0.050	0.201	0.180	0.123	0.136	0.108	0.081	0.064	0.018	0.096	0.074
Haplotype fequency in MDD	0.026	0.250	0.233	0.104	0.116	0.089	0.060	0.035	0.000	0.130	0.116

Major allele = 1, minor allele = 2. Individual *P*-value indicates the best *P*-value among the haplotypes. Significant results ($P < 0.05$) indicated by italics.

$P < 0.05$. Our results suggest that the Ser704Cys SNP of the DISC1 gene might affect human gray matter volume and white matter microstructure, particularly in peri-cingulate area. On the other hand, genotype effects of other SNPs, i.e. SNP1, SNP7 and SNP9 on the brain morphology or white matter microstructure, were not detected.

DISC1 and ERK signaling

ERK signaling and Akt signaling have been implicated in MDD (24,25). Thus, we investigated the possible involvement of DISC1 on ERK and Akt signaling pathways. The endogenous DISC1 function in cortical cultures was examined using small interfering RNA (siRNA) for DISC1, and robust decrease (70%) of endogenous DISC1 protein was confirmed (Fig. 3Aa and d). We found decreased levels of phosphorylation of ERK1/2 (pERK1/2: an activated form of ERK) and phosphorylation of Akt (pAkt: an activated form of Akt) after DISC1-siRNA transfection, suggesting that endogenous DISC1 protein is involved in ERK and Akt activations (Fig. 3Aa–c). In contrast, the levels of total ERK1/2, Akt and TUJ1 (class III β-tubulin, a neuronal marker) proteins were not altered (Fig. 3Aa, quantified data (mean ± SD): ERK1: 1.15 ± 0.22, 0.95 ± 0.27; ERK2: 1.01 ± 0.17, 0.99 ± 0.22; Akt: 1.05 ± 0.06, 1.09 ± 0.04; TUJ1: 1.03 ± 0.07, 1.01 ± 0.07; relative to none; scramble, si-DISC1, respectively).

To examine the effect of Ser704Cys SNP on ERK and Akt signaling, we overexpressed each type of DISC1 protein (sDISC1: DISC1 protein with Ser704; cDISC1: DISC1 protein with Cys704) using a sindbis virus-mediated gene delivery system. Neuronal cultures infected with the control viral construct [green fluorescence protein (GFP) only] were doubly stained with GFP signal and immunostaining signal

Table 3. Gender difference of allele distributions for 13 SNPs in the DISC1 gene among patients with schizophrenia, those with major depression and controls

SNP	female							Male						
	Control	SZ			MDD			Control	SZ			MDD		
	$n = 366$	$n = 318$	P-value	OR	$n = 226$	P-value	OR	$n = 351$	$n = 340$	P-value	OR	$n = 147$	P-value	OR
1	0.135	0.102	0.061	—	0.091	*0.021*	*0.64*	0.108	0.107	0.96	—	0.099	0.65	—
2	0.258	0.274	0.52	—	0.279	0.44	—	0.262	0.254	0.74	—	0.238	0.43	—
3	0.466	0.459	0.80	—	0.465	0.97	—	0.456	0.459	0.91	—	0.442	0.69	—
4	0.344	0.385	0.12	—	0.356	0.68	—	0.359	0.366	0.78	—	0.395	0.29	—
5	0.414	0.399	0.58	—	0.469	0.063	—	0.437	0.421	0.53	—	0.398	0.25	—
6	0.373	0.381	0.77	—	0.354	0.51	—	0.352	0.384	0.22	—	0.378	0.44	—
7	0.404	0.447	0.12	—	0.427	0.44	—	0.405	0.437	0.23	—	0.418	0.69	—
8	0.411	0.390	0.42	—	0.425	0.65	—	0.406	0.384	0.40	—	0.401	0.89	—
9	0.209	0.154	*0.0088*	*1.45*	0.164	0.054	—	0.192	0.190	0.90	—	0.170	0.41	—
10	0.399	0.426	0.31	—	0.442	0.14	—	0.430	0.384	0.08	—	0.432	0.96	—
11	0.328	0.343	0.56	—	0.369	0.14	—	0.343	0.325	0.47	—	0.340	0.92	—
12	0.111	0.137	0.14	—	0.146	0.073	—	0.097	0.107	0.52	—	0.143	*0.035*	*0.64*
13	0.383	0.363	0.46	—	0.363	0.50	—	0.369	0.376	0.77	—	0.401	0.34	—

Minor allele frequencies in controls are shown. SZ, schizophrenia; OR, odds ratio. Significant results ($P < 0.05$) indicated by italics.

Table 4. Demographic information for the brain MRI study

Variables	ser/ser-DISC1 ($n = 86$)	cys-DISC1 carriers ($n = 22$)	P-value
Age	35.1 (11.5)	40.1 (13.8)	0.08
Gender (M/F)	33/53	7/15	0.81
Education years	16.7 (2.8)	16.8 (3.4)	0.89
Full-scale IQ	111.8 (11.5)	109.2 (13.7)	0.39

Cys-DISC1 carriers ($n = 22$): cys/ser-DISC1 ($n = 21$) and cys/cys-DISC1($n = 1$). Mean values (SD) are presented.

by anti-microtubule-associated protein 2 (MAP2: a neuronal dendritic marker) antibody, as well as viral constructs of two types of DISC1 (sDISC1 and cDISC1) (Fig. 3Ba). About 85% of MAP2-positive cells in control-, sDISC1- or cDISC1-infected cortical cultures were GFP positive, indicating that the majority of neurons were infected, respectively [control (mean ± SD): 84.4 ± 6.4%; sDISC1: 86.6 ± 5.1%; cDISC1: 86.3 ± 9.8%, n=6 fields, selected randomly]. When cortical cultures infected by sDISC1 or cDISC1 were doubly stained with GFP signal and immunostaining signal by the DISC1 antibody, the sDISC1 and cDISC1 proteins were located in both cell body and neurites in punctuate manner, especially perinuclear region and neurite branch (Fig. 3Bb). As expression levels of GFP and TUJ1 were not altered by viral infections and both sDISC1- and cDISC1-infected cultures showed similar levels of DISC1 expression (Fig. 3Ca, quantified data (mean ± SD): GFP: 1.00 ± 0.10, 0.92 ± 0.15; TUJ1: 0.98 ± 0.07, 0.98 ± 0.09; DISC1: 5.43 ± 0.52, 5.43 ± 0.33, relative to control, sDISC1, cDISC1, respectively), we examined the phosphorylation of ERK and Akt in this system. Two-way ANOVA indicated significant main effects of viral infection ($F = 202$, $df = 2$, $P < 0.001$) and measurement of protein levels ($F = 161$, $df = 8$, $P < 0.001$) and interaction of these two factors ($F = 44.4$, $df = 16$, $P < 0.001$). There were significant effects of viral infection in the measurements of pERK1/2 and pAkt; however, neither total ERK1/2 nor Akt was altered after virus infection (pERK1: $F = 104$, $P < 0.001$; pERK2: $F = 29.2$, $P < 0.001$; pAkt: $F = 9.0$, $P < 0.01$; ERK1: $F = 1.8$, $P > 0.2$; ERK2: $F = 3.0$, $P > 0.1$; Akt: $F = 0.2$, $P > 0.8$) (Fig. 3C). *Post hoc* comparison revealed significant increases in pERK1/2 in sDISC1- or cDISC1-infected cultures compared with control (pERK1: sDISC1 $P < 0.01$; cDISC1 $P < 0.01$; pERK2: sDISC1 $P < 0.05$; cDISC1 $P < 0.05$) (Fig. 3Ca and b). The levels of ERK1 activation in sDISC1-overexpressing cultures were more intensive than those in cDISC1-overexpressing cultures ($P < 0.01$) (Fig. 3Ca and b). A significant elevation of pAkt was observed in the sDISC1-overexpressing cultures compared with control ($P < 0.05$), although an increase in the pAkt level by cDISC1 overexpression was not significant ($P > 0.1$) (Fig. 3Ca and c). However, there were no significant difference of pAkt levels between sDISC1 and cDISC1 ($P > 0.1$).

We next examined rescue experiments, transfection with sDISC1 or cDISC1 into primary culture knocked down to DISC1. In this experiment, siRNA for DISC1 decreased phosphorylation of ERK by ~50% and there were significant effects of viral infection in the measurements of pERK1/2 (pERK1: $F = 7.3$, $P < 0.01$; pERK2: $F = 9.4$, $P < 0.01$) (Fig. 3D). *Post hoc* comparison revealed a significant elevation of pERK1 levels in the sDISC1-overexpressing cultures compared with si-DISC1 treatment ($P < 0.01$), although an increase in the pERK1 level by cDISC1 overexpression was not statistically significant ($P > 0.1$) (Fig. 3D). A significant elevation of pERK2 was observed in sDISC1- and cDISC1-infected cultures compared with si-DISC1 treatment (sDISC1: $P < 0.05$; sDISC1: $P < 0.05$) (Fig. 3D). Western blots showed that total ERK, Akt and TUJ1 protein levels were not changed and that pAkt levels were also rescued by DISC1 overexpression (Fig. 3Da). These results suggest the recovery of the activation of ERK1/2 and Akt after sDISC1- and cDISC-overexpression in DISC1 knockdown cultures. The effect of rescue on phosphorylation of ERK was larger in sDISC1 compared with cDISC1, although the difference did not reach the statistical significance (Fig. 3D). This

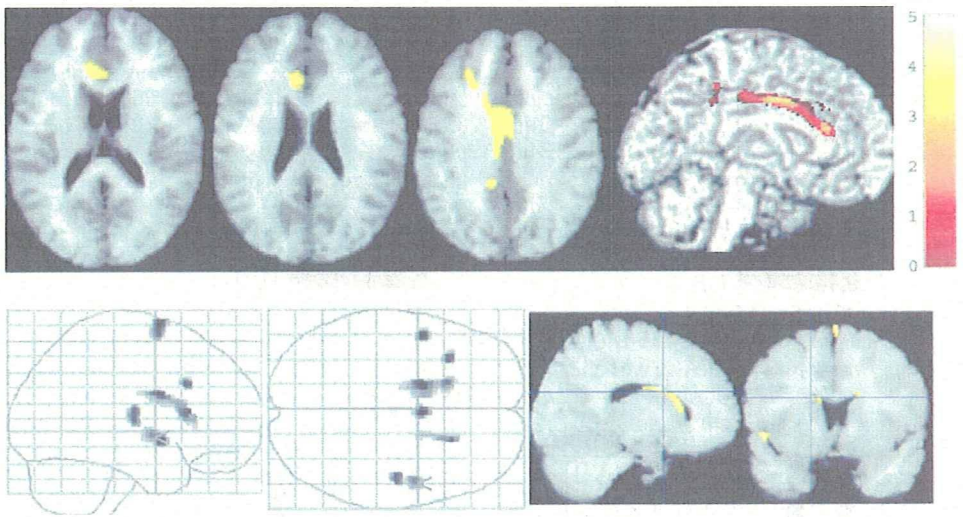

Figure 1. Impact on the brain morphology of the Ser704Cys SNP in healthy subjects. (Upper panel) The SPM {t} is displayed onto T1-weighted MR images. Cys-DISC1 carriers ($n = 22$) had reduced volumes in the bilateral ACC, cingulate gyrus and the posterior cingulate gyrus compared with ser/ser-DISC1 individuals ($n = 86$). (Lower panel) The SPM{t} is displayed on a standard maximum intensity projection images and T1-weighted MR images. Ser/Ser-DISC1 individuals demonstrated decreased volumes of the lateral ventricle, interhemispheric fissure and bilateral Sylvian fissure, indicating an expansion of the CSF space in cys-DISC1 carriers.

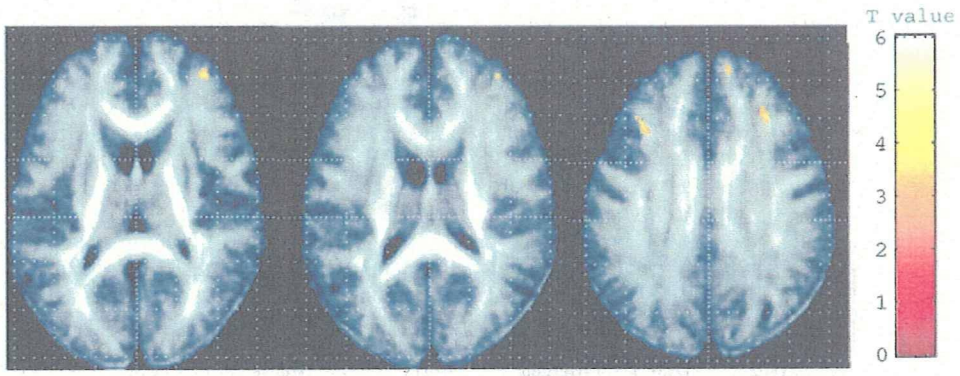

Figure 2. Disruption of white matter integrity revealed by DTI. The SPM{t} is displayed onto a FA map. A significant reduction in FA in the prefrontal white matter was found in the cys-DISC1 carriers ($n = 22$) when compared with individuals with ser/ser-DISC1 ($n = 86$).

might be due to the complexity of this experiment (siRNA plus overexpression) compared with the overexpression only experiments, as the standard deviations of these experiments were larger than those of overexpression experiments. Our results suggest a possible role of DISC1 in the ERK and Akt signaling and an impact of Ser704Cys on ERK activation.

DISCUSSION

Here, we report the evidence for association between MDD and the Ser704Cys SNP as well as several haplotypes including the Ser704Cys SNP. We also replicated earlier evidence for a weak association with schizophrenia which is stronger in female patients (4). Previous association studies with schizophrenia suggested several regions in the DISC1 gene, such as intron2–intron3, intron4–intron9 and intron9–exon13 (4, 5, 8, 9). The region of intron8–intron9 is common across the studies. Consistent with the previous studies, two SNPs in intron9 were associated with schizophrenia in our study. Both false-positive and false-negative associations due to population stratification cannot be excluded in our case–control study, despite the precaution of ethnic matching of this study. Differences in gender ratio and ages between groups could be potential confounding factors. Therefore, it is necessary to carry out further investigations to confirm our findings in other samples. It has also suggested that allelic heterogeneity exists for association between the DISC1 gene and psychiatric illness (26), and this may explain different alleles being associated with illness in our sample compared with others.